Article:
Pedatella, NM, Liu, H, Marsh, DR et al. (2019) Error growth in the Mesosphere and Lower Thermosphere Based on Hindcast Experiments in a Whole Atmosphere Model. Space Weather, 17 (10). pp. 1442-1460. ISSN: 1542-7390

https://doi.org/10.1029/2019sw002221

AGU100 ADVANCING EARTH AND SPACE SCIENCE

Space Weather

RESEARCH ARTICLE
10.1029/2019SW002221

Special Section:
Scientific Challenges of Space Weather Forecasting Including Extremes

Error growth in the Mesosphere and Lower Thermosphere Based on Hindcast Experiments in a Whole Atmosphere Model

N. M. Pedatella[1,2], H.-L Liu[1], D. R. Marsh[1,3,4], K. Raeder[5], and J. L. Anderson[5]

[1]High Altitude Observatory, National Center for Atmospheric Research, Boulder, CO, USA, [2]COSMIC Program Office, University Corporation for Atmospheric Research, Boulder, CO, USA, [3]Atmosphere Chemistry Observations and Modeling, National Center for Atmospheric Research, [4]School of Physics and Astronomy, University of Leeds, Leeds, UK, [5]Computational and Information Systems Laboratory, National Center for Atmospheric Research, Boulder, CO, USA

Key Points:
- Mesosphere and lower thermosphere error growth rate increases with increasing altitude
- Errors in zonal mean and large scale waves grow more slowly than errors in small-scale waves
- At altitudes relevant for space weather forecasting, the error in atmospheric tides saturates after approximately 5 days

Correspondence to:
N. M. Pedatella,
nickp@ucar.edu

Citation:
Pedatella, N. M., Liu, H.-L., Marsh, D. R., Raeder, K., & Anderson, J. L. (2019). Error Growth in the Mesosphere and Lower Thermosphere Based on Hindcast Experiments in a Whole Atmosphere Model. *Space Weather*, *17*, 1442–1460. https://doi.org/10.1029/2019SW002221

Received 10 APR 2019
Accepted 12 SEP 2019
Accepted article online 9 OCT 2019
Published online 24 OCT 2019

Abstract The capability to forecast conditions in the mesosphere and lower thermosphere is investigated based on 30-day hindcast experiments that were initialized bimonthly during 2009 and 2010. The hindcasts were performed using the Whole Atmosphere Community Climate Model with thermosphere-ionosphere eXtension (WACCMX) with data assimilation provided by the Data Assimilation Research Testbed (DART) ensemble Kalman filter. Analysis of the WACCMX+DART hindcasts reveals several important features that are relevant to forecasting the middle atmosphere. The results show a clear dependence on spatial scale, with the slowest error growth occurring in the zonal mean and the fastest error growth occurring for small-scale waves. The error growth rate is also found to be significantly greater in the upper mesosphere and lower thermosphere compared to in the upper stratosphere to lower mesosphere, suggesting that the forecast skill decreases with increasing altitude. The results demonstrate that the errors in the lower thermosphere reach saturation, on average, in less than 5 days, at least with the current version of WACCMX+DART. A seasonal dependency to the error growth is found at high latitudes in the Northern and Southern Hemispheres but not in the tropics or global average. We additionally investigate the error growth rates for migrating and nonmigrating atmospheric tides and find that the errors saturate after ~5 days for tides in the lower thermosphere. The results provide an initial assessment of the error growth rates in the mesosphere and lower thermosphere and are relevant for understanding how whole atmosphere models can potentially improve space weather forecasting.

Plain Language Summary The ionosphere and thermosphere are known to vary significantly from day to day, and this day-to-day weather is driven by processes originating in the lower atmosphere (below 50 km), especially during periods of quiet solar activity. Accurate forecasting of the ionosphere-thermosphere variability thus partially depends on the ability to forecast the component that originates in the lower atmosphere. This study makes use of recent developments in whole atmosphere models to provide the first comprehensive investigation of current capabilities to forecast the lower atmospheric drivers of ionosphere-thermosphere day-to-day variability. We evaluate the error growth of a whole atmosphere-ionosphere model with data assimilation (WACCMX+DART) at altitudes (60–120 km) that are relevant for generating the day-to-day variability in the ionosphere and thermosphere. We demonstrate that the error growth rate is larger at higher altitudes, and for smaller spatial scales. Furthermore, it is found that, on average, the error growth in the primary drivers of spatial and temporal variability in the ionosphere saturates after approximately 5 days. The forecast skill of the ionosphere is typically thought to be less than 24 hr; however, the present study illustrates that the forecast skill of the ionosphere can potentially be increased by incorporating forecasts of the lower atmospheric drivers.

1. Introduction

The ability to forecast conditions in the ionosphere and thermosphere is of increasing relevance due to a growing dependence upon space-based assets, as well as satellite communications and navigation. The ionosphere and thermosphere represent a primarily externally driven system, meaning that accurate

predictions of ionosphere and thermosphere variability require predictions of the external drivers (e.g., Siscoe & Solomon, 2006). Considerable efforts have focused on forecasting solar wind conditions, and the magnetosphere-ionosphere coupling that can drive large disturbances in the ionosphere and thermosphere (Cash et al., 2015; Glocer et al., 2016; Liemohn et al., 2018; Merkin et al., 2007; Morley et al., 2018; Owens et al., 2014). The ionosphere and thermosphere are also driven by the ubiquitous waves that propagate upwards from the lower atmosphere (troposphere and stratosphere), as well as those that are generated in situ due to wave dissipation and wave-wave interactions. These waves drive ionosphere and thermosphere variability across a range of spatial and temporal scales, ranging from minutes to days and 10 to 1,000 s of kilometers (Liu, 2016). They may also influence how the ionosphere and thermosphere respond to geomagnetic storms (Hagan et al., 2015; Pedatella & Liu, 2018).

Relatively little is known about the current capabilities to forecast conditions in the mesosphere and lower thermosphere (MLT). This is despite the fact that the variability in the MLT is an important driver of ionosphere and thermosphere variability. The predictability and error growth characteristics of the MLT were investigated by Liu et al. (2009) and Smith et al. (2017) using the Whole Atmosphere Community Climate Model (WACCM). Both studies found that inability to constrain small-scale waves is an important source of the error growth. Liu et al. (2009) also found that the predictability depends on season and altitude, with largest error growth occurring in the high latitude, wintertime, MLT. It is important to note that both Liu et al. (2009) and Smith et al. (2017) investigated the predictability of the MLT using what are often referred to as perfect model experiments, which neglect aspects such as errors in initial conditions and model errors that would be present in true forecasts. They thus provide what may be considered as an upper limit on the potential forecast skill at MLT altitudes. Nezlin et al. (2009) investigated the MLT predictability based on assimilating observations in the lower atmosphere and found that the assimilation of troposphere and stratosphere observations leads to MLT predictability on large scales. It should, however, be noted that this conclusion is based on reproducing a simulated truth and that the control of the MLT by the troposphere-stratosphere was partly disputed by Smith et al. (2017), who found that there is less control of the MLT by the troposphere-stratosphere in a model with more complex gravity wave drag parameterization. More realistic hindcasts of the middle and upper atmosphere variability during the 2009 sudden stratospheric warming (SSW) time period were performed by Wang et al. (2014) and Pedatella et al. (2018). Both studies found that the SSW, and resulting effects in the MLT and ionosphere, could be forecast 5–10 days in advance of the SSW central date, defined as the reversal of the zonal mean zonal winds at 10 hPa and 60° N. Though illustrating the potential of extremely good forecast skill in the MLT, these studies may not be wholly representative since SSWs can be forecast 5-15 days in advance (e.g., Karpechko, 2018; Tripathi et al., 2015), and they produce large disturbances in the middle and upper atmosphere.

The development of models with data assimilation capabilities that extend into the lower thermosphere enables initialization of forecasts that extend into the MLT. Examples of such models include the Canadian Middle Atmosphere Model (CMAM; Nezlin et al., 2009; Polavarapu et al., 2005; Ren et al., 2011), the Navy Operational Global Atmosphere Prediction System—Advanced Level Physics High Altitude (NOGAPS-ALPHA) and Navy Global Environment Model (NAVGEM; Eckermann et al., 2009, 2018), WACCM (Pedatella et al., 2014), and the Whole Atmosphere Model (WAM; Wang et al., 2012). Though these models all extend into the MLT, they use different data assimilation techniques. It should also be noted that not all assimilate MLT observations, potentially limiting the fidelity of analyses and forecasts of the MLT. To date, these systems have primarily been used for research studies based on their high-quality analysis fields (e.g., France et al., 2018; Gu et al., 2016; Lieberman et al., 2015; Siskind et al., 2011). The extent that they have been used to investigate forecast skill in the MLT is limited to the previously mentioned SSW case studies (Pedatella et al., 2018; Wang et al., 2014), or short-term (6 hr) observation minus forecast statistics (Hoppel et al., 2013; Nezlin et al., 2009).

The present study provides the first thorough evaluation of the error growth in the MLT using a set of initialized hindcast experiments. Using the Whole Atmosphere Community Climate Model with thermosphere-ionosphere eXtension (WACCMX) with data assimilation provided by the Data Assimilation Research Testbed (DART) ensemble Kalman filter, we present the analysis of 30-day ensemble hindcasts that were initialized on the 1st and 15th of each month during 2009 and 2010. The hindcast experiments are used to investigate various aspects of the error growth in the middle atmosphere, including the altitude, season, and scale-size dependence. The error growth of atmospheric tides is also investigated. The results

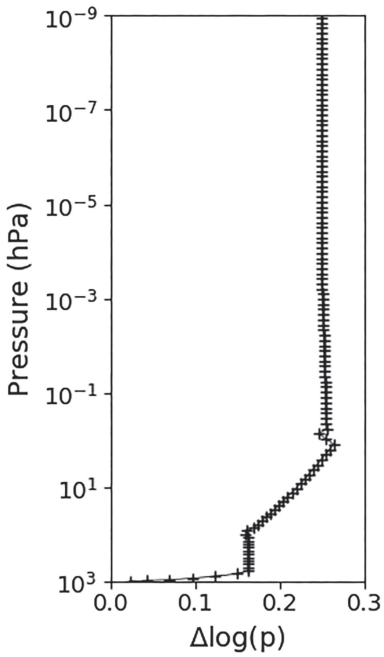

Figure 1. WACCM-X vertical resolution in *log*(*p*) coordinates as a function of height.

provide insight into the current capabilities of WACCMX+DART to potentially forecast conditions in the middle atmosphere.

The remainder of the paper is organized as follows. In section 2 WACCMX+DART is described along with the configuration for the hindcast experiments. Results are presented in section 3 and are discussed in section 4. Conclusions of the study are given in section 5.

2. WACCMX+DART Analysis and Hindcast Experiments

An identical setup as Pedatella et al. (2018) is used to generate the WACCMX+DART analysis fields and to perform the hindcast experiments. The main aspects of WACCMX+DART are summarized in the following, and the reader is referred to Pedatella et al. (2018) for additional details. The forecast model is WACCMX version 2.0 (Liu et al., 2018), which is a whole atmosphere general circulation model extending from Earth's surface to the upper thermosphere (4.1×10^{-10} hPa, ~500–700 km). WACCMX version 2.0 is based on WACCM version 4 (Marsh et al., 2013), which extends the Community Atmosphere Model (CAM) version 4 (Neale et al., 2013) into the lower thermosphere. The model horizontal resolution is 1.9° in latitude and 2.5° in longitude. In the vertical direction, WACCMX uses a hybrid σ-p coordinate system and is purely pressure based above 100 hPa. The vertical resolution in *log*(*p*) coordinates varies from ~0.16 in the troposphere and lower stratosphere to 0.25 in the mesosphere and thermosphere (Figure 1).

The data assimilation is performed using the DART ensemble adjustment Kalman filter (Anderson, 2001; Anderson et al., 2009). Similar to previous studies (Pedatella et al., 2014; Pedatella et al., 2018), the WACCMX+DART experiments in the present study are performed using 40 ensemble members. Spatially and temporally varying adaptive inflation (Anderson, 2009) is applied, with the inflation damping set to 0.7 and lower bound of 0.6 for the inflation standard deviation. The assimilation frequency is 6 hr. The observations assimilated include conventional meteorological observations (i.e., aircraft temperatures, radiosonde temperatures, and winds), Global Positioning System (GPS) radio occultation refractivity, and temperature observations from the Aura Microwave Limb Sounder (MLS) and Thermosphere Ionosphere Mesosphere Energetics Dynamics (TIMED) satellite Sounding of the Atmosphere using Broadband Emission Radiometry (SABER) instrument. Due to the bias between SABER and MLS temperatures (e.g., Hoppel et al., 2008), we adjust the SABER temperatures based on the altitude-dependent mean difference between SABER and MLS temperature observations.

The present study focuses on the 2009–2010 time period, a deep solar minimum period when the upper atmosphere is expected to be significantly influenced by coupling with the lower atmosphere. WACCMX+DART analysis fields were generated from 1 December 2008 to 31 December 2010. The initial ensemble was produced by adding small perturbations to the temperature and wind fields from a single instance, free-running, transient WACCMX simulation on 1 October 2008. The analysis fields were used as initial conditions to perform 30-day hindcasts initialized on the 1st and 15th of each month from January 2009 to December 2010, with the exception that we do not perform a hindcast initialized on 15 December 2010. We thus include a total of 47 hindcast experiments in the present analysis. The hindcasts were performed as initialized, free-running, WACCMX simulations, and no additional perturbations or inflation were applied during the 30-day hindcast period. Note that each hindcast consisted of 40 ensemble members, though we primarily limit our analysis to the ensemble means in the present study. The hindcast experiments use analyzed sea surface temperatures (SSTs) (Hurrell et al., 2008) that are unperturbed, and identical to those used in the WACCMX+DART analysis experiments. This may lead to a slight improvement in the hindcasts compared to true forecasts. However, for the time range investigated in the present study (<30 days), the forecast skill of SSTs is high (Sooraj et al., 2012), and we thus anticipate any impact of using analyzed SSTs instead of forecast SSTs to be small. The sea ice is also prescribed in the hindcast experiments, and the land model is coupled to the atmosphere. As in Pedatella et al. (2018), the hindcast

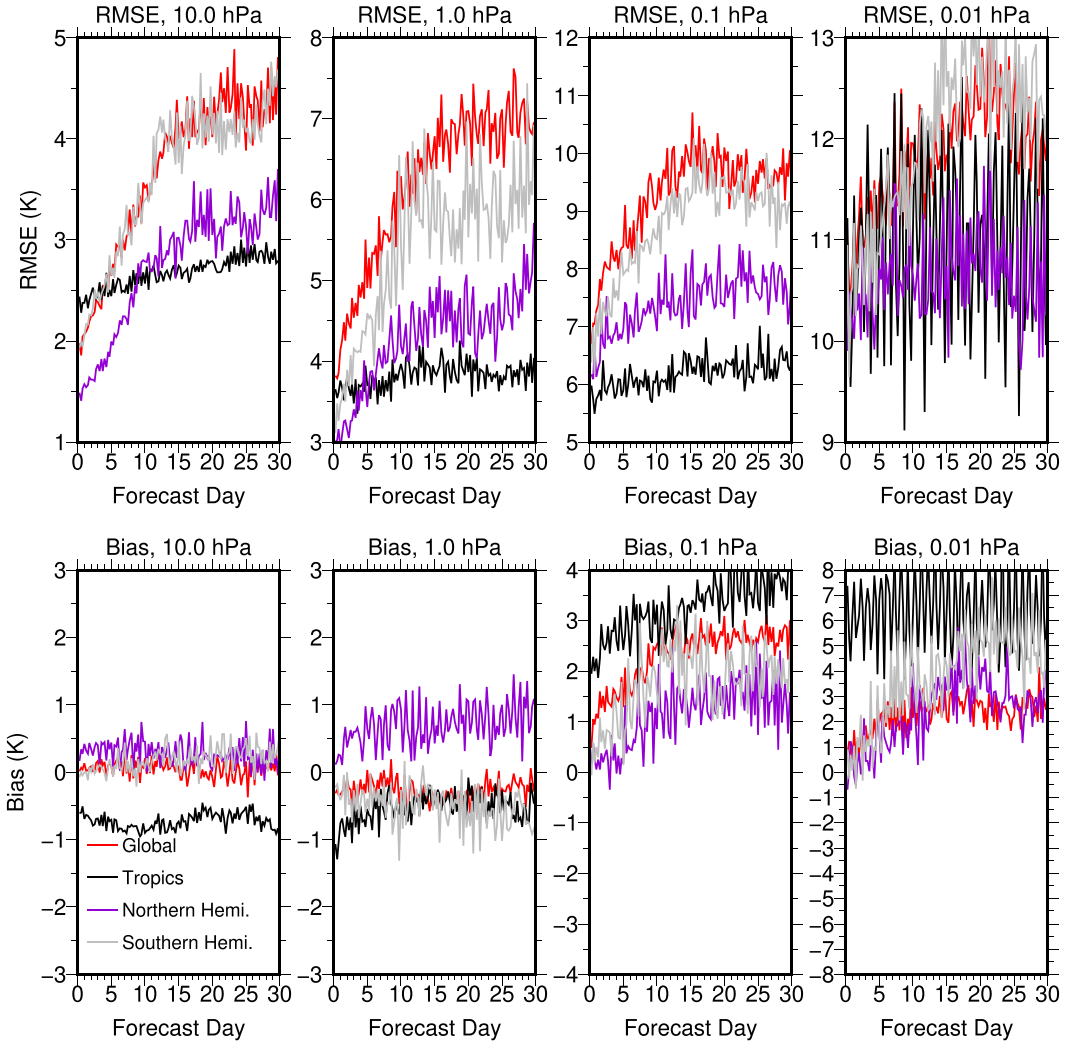

Figure 2. Root mean square error (top) and bias (model observation; bottom) of WACCMX+DART hindcast experiments verified against Aura MLS temperature observations at different altitudes. Results are based on the median of all hindcast experiments.

experiments use 27-day lagged solar and geomagnetic activity, which are parameterized by the F10.7-cm solar radio flux and geomagnetic K_p index, respectively. Note that this is equivalent to a persistence forecast of solar and geomagnetic activity based on the average solar rotation period. Differences between the true and forecast solar and geomagnetic activity should have minimal influence on the results of the present study, though they would be relevant at higher altitudes.

The identical model configuration is used for both the analysis and hindcast experiments. That is, we use the same WACCMX dynamics, chemistry, and physics. To reduce the impact of small-scale waves introduced by the data assimilation adjustments, Pedatella et al. (2018) added additional second-order divergence damping (Lauritzen et al., 2012) to the existing fourth-order divergence damping in WACCMX. The second-order divergence damping coefficient (τ) used in WACCMX+DART is given by $\tau = \frac{1}{128}\max\{1, 4[1+\tanh(\log(\frac{10^{-4}}{p_k})]\}$, where p_k is the pressure in hPa at the center of the model level. The additional damping is included for model stability, and to reduce the additional mixing due to small-scale waves that leads to a decrease in thermosphere O/N_2 and ionosphere electron density. The second-order divergence damping is also applied in the hindcast experiments. This may lead to greater damping in the hindcast experiments than necessary and has potential implications on the hindcasts, especially since the small-scale waves introduced by the data assimilation decay after a few days. Global-scale waves may also be overly damped in

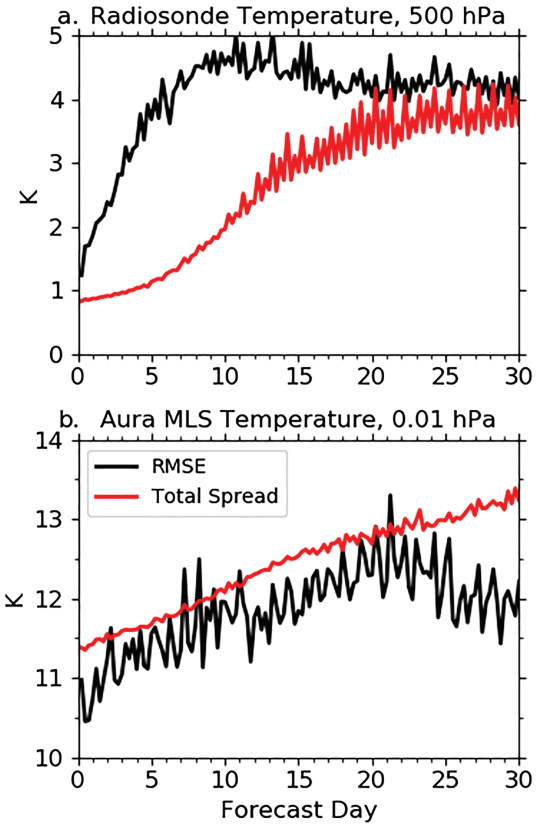

Figure 3. Global root mean square error and total spread for radiosonde temperature at 500 hPa (top) and Aura MLS temperature at 0.01 hPa (bottom). Results are based on the median of all hindcast experiments.

the hindcast experiments since the extra damping is no longer compensated by the assimilation of satellite observations in the MLT.

3. Results

The root mean square error (RMSE) and bias (model observation) of the WACCMX+DART hindcasts relative to Aura MLS temperature observations in the stratosphere and mesosphere are shown in Figure 2. The RMSE here, and throughout the remainder of the paper, is calculated without removal of the mean. The results are separated by region, and the results in Figure 2 are the median of all of the hindcast experiments. The regions are defined as global (90° S-90° N), tropics (20° S-20° N), Northern Hemisphere (60–90° N), and Southern Hemisphere (60–90° S) high latitudes. Note that the results in Figure 2 are based on all available Aura MLS temperature profiles, and the vertical averaging kernel of the Aura MLS observations is not considered in this comparison (or in the assimilation of the MLS temperature observations). Aura MLS observations are Sun-synchronous at ~1:30 and 13:30 local time. The results in Figure 2 thus only provide verification of the hindcasts at these local times. Similar results are obtained for comparison of the hindcast experiments with SABER temperatures (not shown). The most notable feature in Figure 2 is that the RMSE and bias tend to increase with increasing altitude (note the different vertical scales for each panel). The error grows faster and tends to reach saturation sooner, at higher altitudes. For example, at 10.0 hPa, the global RMSE grows nearly linearly for ~20 days at a rate of ~0.1 K/day, while at 0.1 hPa the error grows at a rate of ~0.17 K/day and nearly saturates after 15 days. This behavior is consistent with previous investigations of predictability in perfect model experiments (Liu et al., 2009). There is also a clear difference in the behavior in the tropical region, with lower RMSE values and slower error growth below 0.1 hPa. The reason for this is unknown, though it may be partly related to the sparsity of observations in the tropics due to the polar orbit of the Aura satellite. It may also be related to less short-term dynamical variability in the tropical stratosphere compared to the higher latitudes. There are also clear sub-daily oscillations in both the RMSE and bias, which increase in amplitude at higher altitudes. These oscillations are believed to be due to deficiencies in the atmospheric tides, in particular the nonmigrating tides, which would lead to a UT dependence of the RMSE and bias. In all regions, the temperature bias remains relatively stable (within ~1 K) over the 30-day hindcast period in the stratosphere but drifts by several Kelvin during the initial ~10–20 days of the hindcasts in the mesosphere. The growth of the temperature bias in the mesosphere illustrates that assimilation of mesospheric temperature observations is useful in correcting temperature biases in the forecast model that are related to deficiencies in key physical and subgrid scale dynamical parameterizations, such as the gravity wave drag parameterizations (Hoppel et al., 2013; Pedatella et al., 2014).

Though the present analysis focuses primarily on the ensemble means, it is useful to briefly discuss the ensemble spread. Figure 3 shows the global RMSE and total spread (square root of combined model and observation variance) for radiosonde temperature at 500 hPa and Aura MLS temperature at 0.01 hPa. In the troposphere, the spread is significantly below the RMSE, indicating that the hindcast ensembles are spread deficient. The lack of spread at short lead times is attributed to the use of a reduced adaptive inflation damping coefficient (0.7, instead of the more typical 0.9 used in other DART applications) in the assimilation. At longer lead times, the lack of growth in the spread may indicate the need to also include additional perturbations to the ensemble so that the spread grows at a faster rate. It should be noted that the sub-daily oscillations seen in the radiosonde temperature RMSE and total spread exhibit a clear UT dependence and arise due to the comparison being performed against a different observational network at 0000 and 1200 UT compared to 0600 and 1800 UT. At higher altitudes (Figure 3b), the RMSE and total spread relative to Aura MLS temperature observations are roughly equivalent. This indicates that despite the lack of spread in the troposphere, WACCMX+DART generates sufficient spread at higher altitudes.

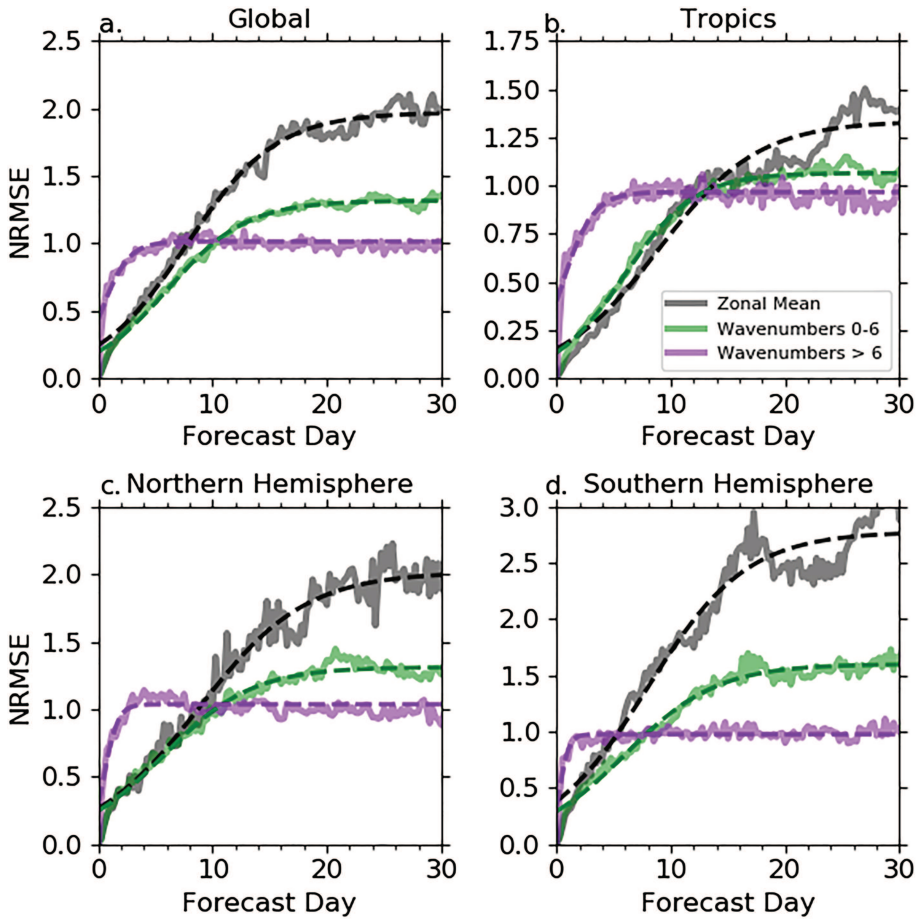

Figure 4. Normalized root mean square error in zonal wind at 0.1 hPa in different regions: (a) global, (b) tropics (20° S-20° N), (c) Northern Hemisphere (60-90° N), and (d) Southern Hemisphere (60-90° S). The results are based on verifying the WACCMX+DART hindcast experiments against the WACCMX+DART analysis fields. Solid lines indicate the median of all hindcast experiments, and thick dashed line is the best fit error growth curve.

The limited observations in the MLT prevent an in-depth verification of the hindcasts using only observations. In the remainder of the paper we thus use the analysis fields from WACCMX+DART to verify the hindcasts. The verification is performed every 6 hr (0000, 0600, 1200, and 1800 UT), which corresponds to the assimilation frequency. Figures 4 and 5 show the median normalized RMSE (NRMSE) at 0.1 and 0.01 hPa, respectively, for the zonal wind in different regions. The NRMSEs are based on normalizing the RMSE for each individual hindcast with the RMSE based on a 38-year (1980–2017) climatology from specified dynamics WACCMX (SD-WACCMX). Note that we correct for biases between the SD-WACCMX and WACCMX+DART analysis by removing the mean difference at each latitude and altitude. The RMSE for each 30-day hindcast is calculated based on the ensemble means of the hindcast and analysis fields (i.e., we do not make use of individual ensemble members). By normalizing the hindcasts with the climatological RMSE, a NRMSE value less than one indicates that the hindcast is better than climatology, at least in comparison to the analysis fields. Note that throughout the following we use the NRMSE in order to more easily compare the error growth characteristics across different altitudes, scale-sizes, and seasons. The solid lines in Figures 4 and 5 indicate the median NRMSE of all the hindcast experiments. To investigate any dependence on spatial scale, the NRMSE is calculated separately for the zonal mean (black), wavenumbers 0–6 (green), and wavenumbers greater than 6 (violet). In the remainder of the paper, we consider large-scale waves to be the wavenumbers 0–6 and small-scale waves to be wavenumbers greater than 6. The use of the WACCMX+DART analysis fields to verify the hindcasts may influence the results, especially for small-scale waves which may not be well constrained by observations at MLT altitudes. Verification by analysis fields is, however, a standard approach in numerical weather prediction, and we believe appropriate for the present study given the lack of comprehensive observations at MLT altitudes that can be used for verification. Since

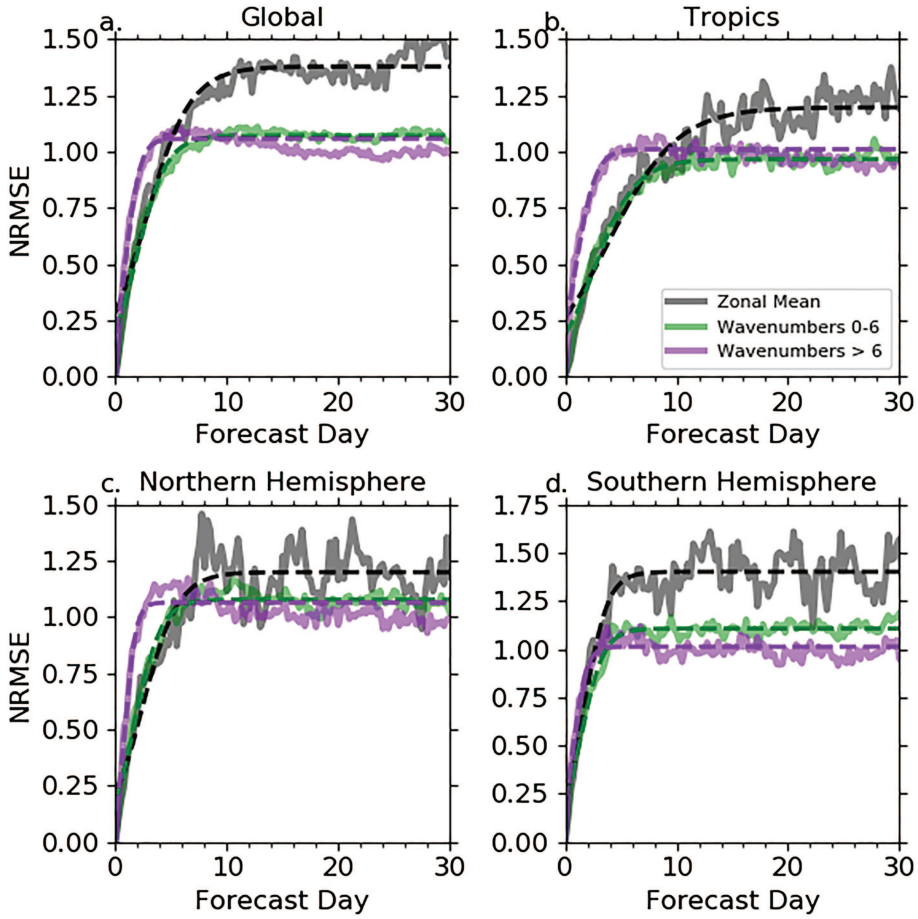

Figure 5. Same as Figure 4, except at 0.01 hPa.

the analysis fields cannot be fully verified on all scales, this approach limits what can be said about the true forecast skill of WACCMX+DART. The results thus primarily provide insight into the error growth rate, and any inferences made about the MLT forecast skill should be considered in light of the fact that the verification is performed against the analysis fields.

The error growth in the hindcasts exhibits the expected behavior with an initial phase of error growth followed by error saturation. The error can be parameterized by a logistic growth curve, with the following

Table 1
Error Growth Rate (α, day^{-1}) for Zonal Wind in the WACCMX+DART Hindcast Experiments Averaged over All Seasons at 0.1 and 0.01 hPa for Different Regions and Spatial Scales

Pressure (hPa)	Wavenumber	Global (α)	Tropics (α)	NH (α)	SH (α)
0.1	0	0.25 ± 0.01	0.23 ± 0.01	0.21± 0.01	0.23 ± 0.01
0.1	0–6	0.29 ± 0.01	0.33 ± 0.01	0.26 ± 0.01	0.25 ± 0.01
0.1	>6	0.86 ± 0.08	0.73 ± 0.07	1.67 ± 0.20	2.44 ± 0.41
0.01	0	0.50 ± 0.03	0.33 ± 0.02	0.63 ± 0.03	0.97 ± 0.09
0.01	0–6	0.74 ± 0.02	0.54 ± 0.02	0.86 ± 0.02	0.98 ± 0.04
0.01	>6	1.57 ± 0.08	1.16 ± 0.07	2.12 ± 0.20	1.74 ± 0.14

Note. Results are given for the best fit values as well as their standard error. Regions are defined as global (90° S-90° N), tropics (20° S-20° N), Northern Hemisphere (60–90° N), and Southern Hemisphere (60–90° S).

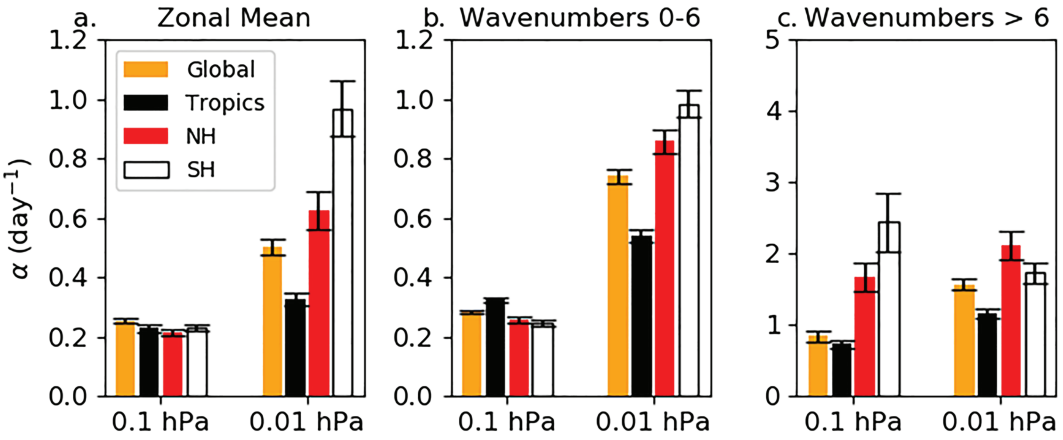

Figure 6. Error growth rate (α) for the (a) zonal mean, (b) wavenumbers 0–6, and (c) wavenumbers greater than 6 in the WACCMX+DART hindcast experiments averaged over all seasons at 0.1 and 0.01 hPa for different regions. Error bars represent the standard error.

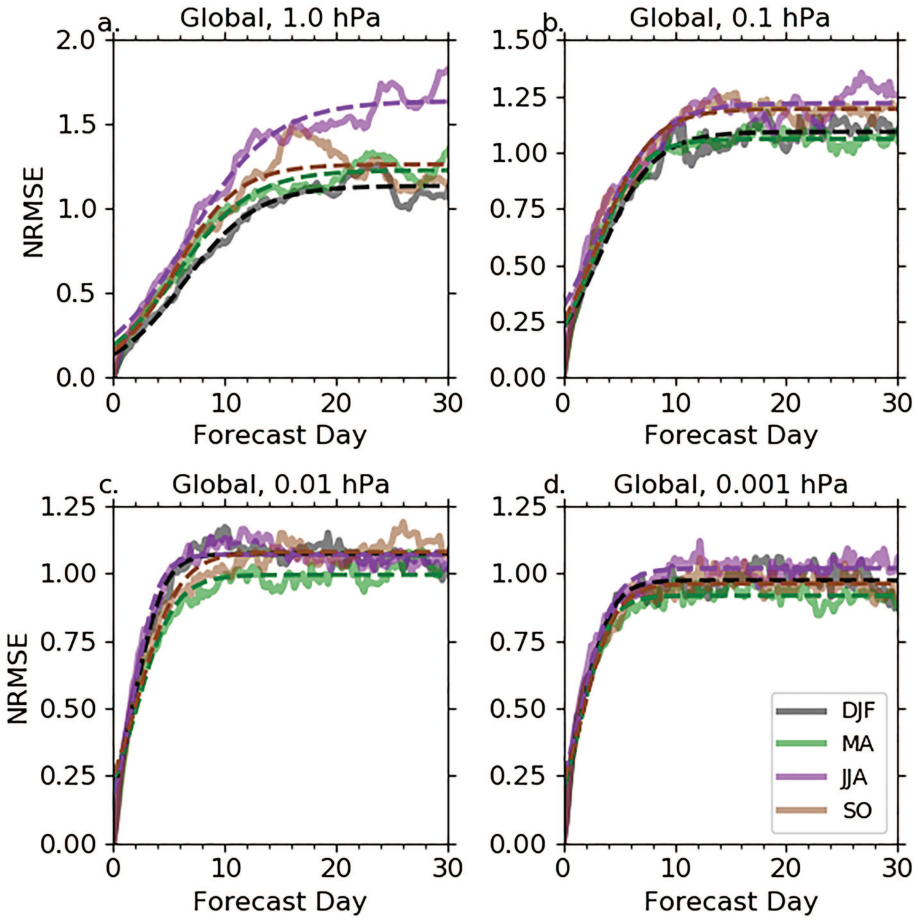

Figure 7. Global normalized root mean square error in zonal wind for wavenumbers 0–6 in different seasons at (a) 1.0, (b) 0.1, (c) 0.01, and (d) 0.001 hPa in WACCMX+DART hindcast experiments verified against WACCMX+DART analysis fields. Solid lines indicate the median of all hindcast experiments, and thick dashed line is the best fit error growth curve.

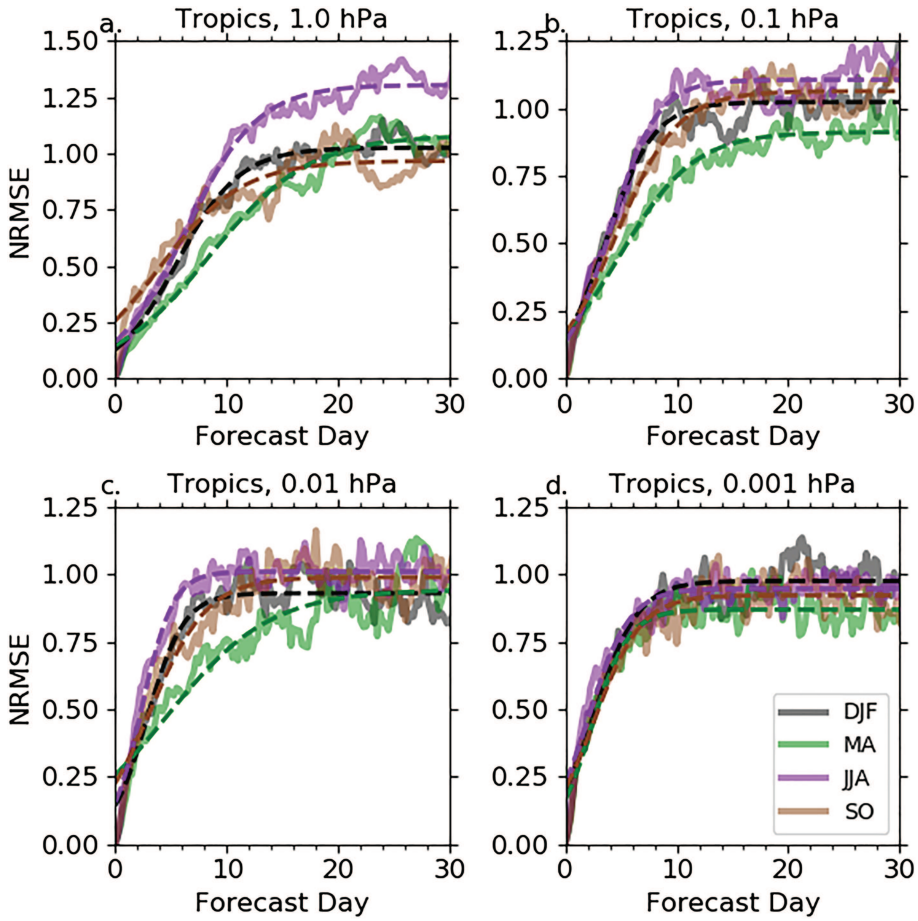

Figure 8. Same as Figure 7, except for in the tropics (20° S-20° N).

equation:

$$e(t) = e_s - \frac{e_s}{1 - \frac{e_0 exp[\alpha t]}{e_0 - e_s}}, \quad (1)$$

where e is the NRMSE, t is time, α is the error growth rate, and e_0 and e_s are the initial and saturation RMSE, respectively (Dalcher & Kalnay, 1987; Savijarvi, 1995). The NRMSE curves are fitted to equation (1) to determine α, e_0, and e_s. The coefficients α are given in Table 1 and Figure 6. The resulting error growth curves are shown by the thick dashed lines in Figures 4 and 5.

Figures 4 and 5, along with Table 1 and Figure 6, reveal several notable features of the hindcast error growth when averaged over all seasons. At both 0.1 and 0.01 hPa, there is a clear dependence on spatial scale. The error growth is fastest for the small-scale waves, and slowest for the zonal mean. The time for the NRMSE to reach 1.0, which corresponds to the RMSE of a climatological forecast, exhibits the corresponding relationship with scale-size, and it is shortest for small-scale waves and longest for the large-scale waves and zonal mean. When averaged over all seasons, there are slightly slower error growth rates in the tropics compared to high latitudes, which is generally consistent with the climatological variability being larger at high latitudes (e.g., Liu et al., 2009; Nezlin et al., 2009). There is additionally a clear hemispheric difference, with slower error growth in the Northern Hemisphere compared to the Southern Hemisphere. This may be due to the sparsity of data in the Southern Hemisphere assimilated in WACCMX+DART, especially given the lack of radiance assimilation. Comparison of Figures 4 and 5 reveals a clear altitude dependence, with faster error growth, and shorter time to reach a NRMSE of 1.0 at 0.01 hPa compared to 0.1 hPa. This suggests that there is a decrease in the forecast skill at higher altitudes. It is important to note that the results for small-scale waves (wavenumbers greater than 6) have high uncertainty due to the large uncertainty in accurately capturing the small-scale waves in the data assimilation system analysis fields, especially at higher altitudes

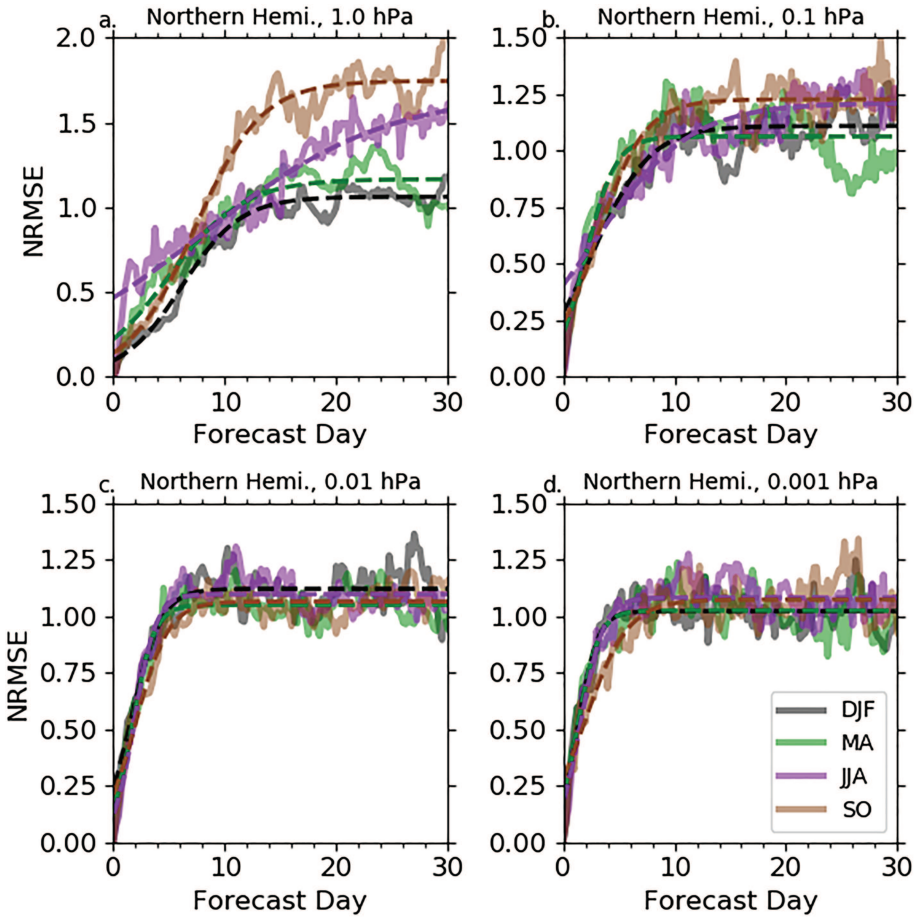

Figure 9. Same as Figure 7, except for in the Northern Hemisphere (60–90° N).

which are only loosely constrained owing to the sparse nature of observations in the MLT. Though we consider it likely that the error growth is faster for small-scale waves, the true error growth rate for these waves remains highly uncertain due to difficulty in completely verifying the smaller-scale structures in the MLT.

The seasonal dependence of the NRMSE for wavenumbers 0–6 in different regions and at different altitudes is shown in Figures 7–10 Corresponding values of α are provided in Table 2 and Figure 11. The results are subdivided into four seasons, December-February (DJF), March-April (MA), June-August (JJA), and September-October (SO). Note that we restrict the equinox periods to 2 months to limit the results to periods directly around the equinox. The altitude dependence of the error growth is clearly seen in Figures 7–10, with slower error growth near the stratopause compared to higher altitudes. This behavior is considered to be related to the different dynamical regimes in the stratosphere and mesosphere, with gravity waves generating unbalanced flow that leads to faster error growth in the MLT (Shepherd et al., 2000; Smith et al., 2017). Globally and in the tropics, there tends to be relatively little seasonal dependence to the error growth rates at all altitudes. There is, however, a slight tendency towards slower error growth in the tropics during MA between 1.0 and 0.01 hPa. Any seasonal dependence at higher altitudes in the mesosphere and lower thermosphere is weak globally and in the tropics. It is again noted that there is a clear altitude dependence, with faster error growth occurring at higher altitudes.

The hindcast NRMSEs exhibit more notable seasonal variability at high latitudes in the Northern and Southern Hemispheres (Figures 9 and 10). The corresponding error growth rates are provided in Figure 11 as well as in Table 2, and more clearly indicate the seasonal and hemispheric differences in the error growth rates. In the Northern Hemisphere at 1.0 and 0.1 hPa, the slowest error growth occurs in JJA. This is largely to be expected due to the generally quiescent nature of the high latitude summertime upper stratosphere and lower mesosphere. The fastest error growth occurs during DJF, MA, and SO, which may be due to model

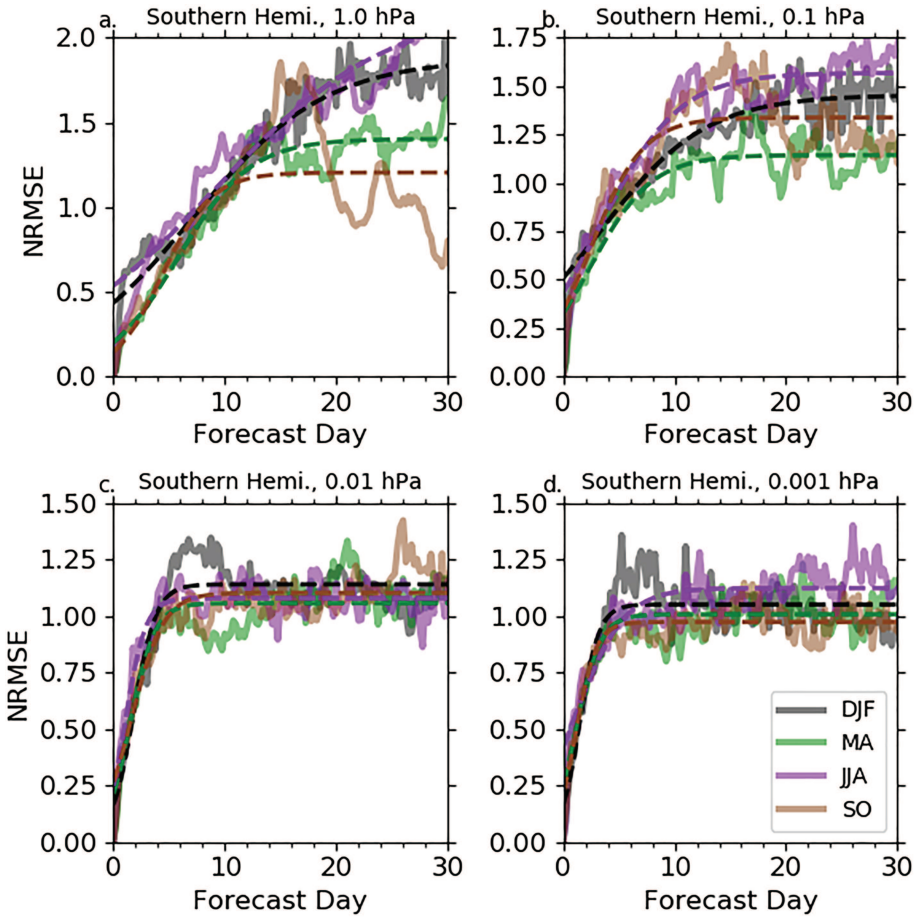

Figure 10. Same as Figure 7, except for in the Southern Hemisphere (60–90° S).

deficiencies in capturing the equinoctial transition as well as the large planetary wave variability during wintertime and equinox time periods (Kleinknecht et al., 2014; Liu et al., 2004; McDonald et al., 2011). In particular, this may be related to the known problem WACCMX has capturing the winter to spring transition, especially in the Southern Hemisphere (e.g., Marsh et al., 2013). At higher altitudes, there is again not a notable seasonal difference in error growth, though there is a tendency towards slower error growth in the Northern Hemisphere during SO. In the Southern Hemisphere, the most notable seasonal dependencies are slower error growth at 0.01 and 0.001 hPa during SO and JJA, respectively. We note that due to the limited nature of the hindcast experiments the results in Figures 7–10 are sensitive to individual hindcasts. This can lead to unusual behavior of the NRMSE, such as the oscillations in the NRMSE that occur during SO in the Southern Hemisphere at 1.0 hPa. The results in Figures 7–10 should thus be considered preliminary since they are based on a limited number of hindcast experiments.

Data assimilation in the MLT is especially critical for controlling the temperature bias that is present in many models that extend into the thermosphere (Hoppel et al., 2013; Pedatella et al., 2014). The evolution of the zonal mean temperature biases (forecast-analysis) at high latitudes in the Northern and Southern Hemisphere in the hindcast experiments during different seasons are shown in Figures 12 and 13, respectively. In the Northern Hemisphere, the zonal mean temperature tends to be relatively stable during MA and JJA and drifts by less than 5–10 K. During other seasons the bias is less stable, and individual hindcasts can exhibit large biases (not shown). The large bias that occurs at 0.1 hPa during DJF may be related to an inability to accurately capture the altitude and magnitude of mesospheric coolings that are associated with SSWs or weakening of the stratospheric polar vortex (e.g., Hoffmann et al., 2007; Zülicke et al., 2018). The hindcast zonal mean temperature biases exhibit more distinct features in the Southern Hemisphere, which shows the development of especially large biases (±10–20 K) during JJA and SO between 1.0 and 0.01 hPa. These can develop within 10 days and may be related to the persistent problem of cold polar stratospheric temperatures

Table 2
Error Growth Rate (α, day^{-1}) for Zonal Wind in the WACCMX+DART Hindcast Eat Different Altitudes, Seasons, and Regions

Pressure (hPa)	Season	Global (α)	Tropics (α)	NH (α)	SH (α)
1.0	DJF	0.31 ± 0.01	0.35 ± 0.01	0.38 ± 0.02	0.17 ± 0.01
1.0	MA	0.30 ± 0.01	0.22 ± 0.01	0.30 ± 0.02	0.31 ± 0.02
1.0	JJA	0.26 ± 0.01	0.31 ± 0.01	0.12 ± 0.01	0.13 ± 0.01
1.0	SO	0.35 ± 0.02	0.27 ± 0.02	0.33 ± 0.01	0.45 ± 0.09
0.1	DJF	0.41 ± 0.02	0.47 ± 0.03	0.39 ± 0.03	0.21 ± 0.01
0.1	MA	0.49 ± 0.02	0.30 ± 0.01	0.74 ± 0.10	0.36 ± 0.03
0.1	JJA	0.37 ± 0.02	0.48 ± 0.02	0.23 ± 0.02	0.28 ± 0.02
0.1	SO	0.42 ± 0.02	0.36 ± 0.02	0.47 ± 0.03	0.43 ± 0.05
0.01	DJF	0.77 ± 0.04	0.60 ± 0.04	0.75 ± 0.07	0.98 ± 0.10
0.01	MA	0.58 ± 0.03	0.21 ± 0.02	1.02 ± 0.09	0.90 ± 0.12
0.01	JJA	0.89 ± 0.04	0.72 ± 0.04	1.05 ± 0.08	1.10 ± 0.11
0.01	SO	0.54 ± 0.03	0.39 ± 0.03	0.69 ± 0.05	0.69 ± 0.08
0.001	DJF	0.77 ± 0.05	0.51 ± 0.03	1.11 ± 0.13	1.14 ± 0.15
0.001	MA	0.78 ± 0.04	0.61 ± 0.04	1.04 ± 0.13	0.90 ± 0.12
0.001	JJA	0.69 ± 0.04	0.55 ± 0.03	0.97 ± 0.10	0.46 ± 0.05
0.001	SO	0.68 ± 0.04	0.47 ± 0.03	0.52 ± 0.05	1.08 ± 0.12

Note. Results are for wavenumbers 0–6. Results are given for the best fit values as well as their standard error. Regions are defined as global (90° S-90° N), tropics (20° S-20° N), Northern Hemisphere (60–90° N), and Southern Hemisphere (60–90° S).

during Southern Hemisphere winter and spring (i.e., the so-called "cold-pole" problem), which are thought to arise due to deficiencies in the gravity wave drag parameterization (Garcia et al., 2017; Marsh et al., 2013).

Atmospheric tides are an important driver of the day-to-day spatial and temporal variability in the ionosphere and thermosphere (e.g., Fang et al., 2013). The ability to forecast tides is thus an important aspect of accurately forecasting the day-to-day space weather. The hindcast median NRMSE for the migrating diurnal (DW1) and semidiurnal (SW2) tides and the nonmigrating eastward propagating diurnal tide with zonal wavenumber 3 (DE3) are shown in Figure 14. The results are for the temperature tides, and the top panel is the RMSE calculated over the altitude range 10-1 hPa, and the bottom panel is for the RMSE calculated over 10^{-3}-10^{-5} hPa. The RMSEs are calculated by using a least-squares fit to determine the tidal amplitudes and phases daily and then reconstructing the temperature field in latitude and longitude at 0000 universal time (UT) for an individual tidal component (e.g., DW1). Hourly output is used for fitting the tides, and the analysis fields thus represent a combination of the analysis and short-term (1–5 hr) forecasts. By reconstructing the tidal field at a given UT, the RMSE accounts for both amplitude and phase errors. Note that since the tides are determined daily, the error on, for example, day one represents errors in the 24- to 48-hr forecast. The RMSE is calculated in the latitudes where the tide obtains large amplitudes (20° S-20° N for DW1, 30° S-30° N for DE3, and 40° S-40° N for SW2). The RMSEs for individual hindcast experiments are normalized by the RMSE of the average analysis tide over the hindcast period. An NRMSE value below 1.0 thus indicates that the hindcast performs better than assuming average tidal behavior. The tidal errors grow rapidly, and the time for the NRMSE to reach 1.0 is less than 5 days. Consistent with the above results, the tidal errors grow faster at MLT altitudes (10^{-3}-10^{-5} hPa) compared to in the upper stratosphere to lower mesosphere (10-1 hPa). In the 10-1 hPa layer, the tidal error growth is slowest for DW1, while at MLT altitudes the slowest error growth occurs in DE3. At both altitudes, there is an especially fast error growth rate of the SW2. The fast error growth for the tides in WACCMX+DART suggests that they may only be predictable out to 2–5 days on average. It should, however, be noted that there is a large spread in the tidal NRMSE, and there are often hindcasts that display slower error growth. Understanding what conditions may lead to slower error growth, and thus enhanced tidal forecast skill, is an important topic for investigation in order to understand when there is better/worse forecast skill of the lower atmospheric drivers of ionosphere-thermosphere variability.

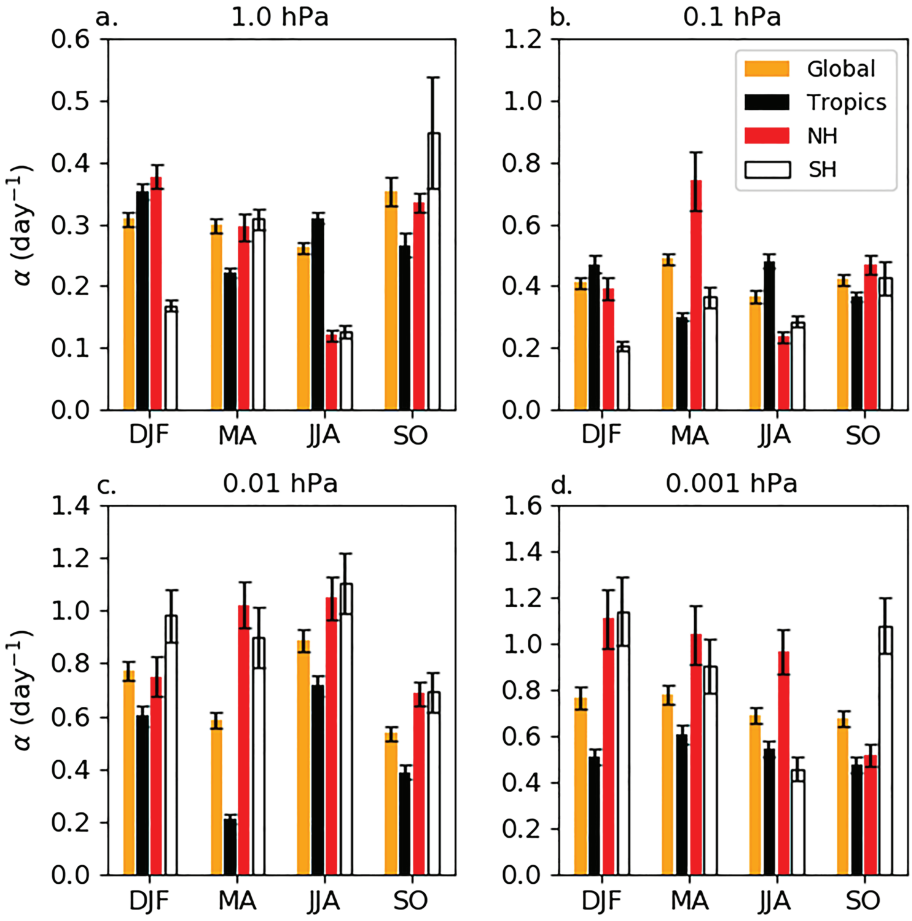

Figure 11. Error growth rate (α) at (a) 1.0, (b) 0.1, (c) 0.01, and (d) 0.001 hPa in the WACCMX+DART hindcast experiments in different seasons and regions. Results are for wavenumbers 0–6. Error bars represent the standard error.

4. Discussion

The results of the present study are generally consistent with previous investigations into the predictability of the middle atmosphere that used perfect model experiments. Liu et al. (2009) similarly found faster error growth at higher altitudes and for smaller scales. They also showed that there was a seasonal variability related to the planetary wave variability, consistent with the results at high latitudes in Figures 9 and 10. Both Liu et al. (2009) and Smith et al. (2017) demonstrated that the error growth due to perturbed initial conditions saturates after 20–30 days. As this number is derived from perfect model experiments, it is representative of the limit of predictability in the middle atmosphere in WACCM. The hindcast experiments presented herein saturate after ~10 days in the MLT, illustrating that there remains considerable room for improvement in terms of forecasting the middle atmosphere. Such improvement may come through improvement in the initial conditions, either by improved data assimilation techniques and/or observations, as well as improvements in the WACCMX model.

There are a number of important short-comings of the present WACCMX+DART hindcast experiments, which should be discussed as they offer potential avenues for improving our initial investigations of the MLT error growth. First, the origins of WACCMX are in climate, not weather, prediction. Many of the processes, such as convective parameterizations and gravity wave drag, have thus been tuned with a focus on longer-term climate instead of short-term weather as would be done for a model focused on numerical weather prediction. Retuning the parameterizations in WACCMX for short-term weather prediction could lead to improved MLT dynamical predictability in WACCMX+DART. It should, however, be noted that there could be some advantages of a model developed based on climate for longer time scales, such as sub-seasonal to seasonal predictions. The current assimilation scheme in WACCMX+DART is another area

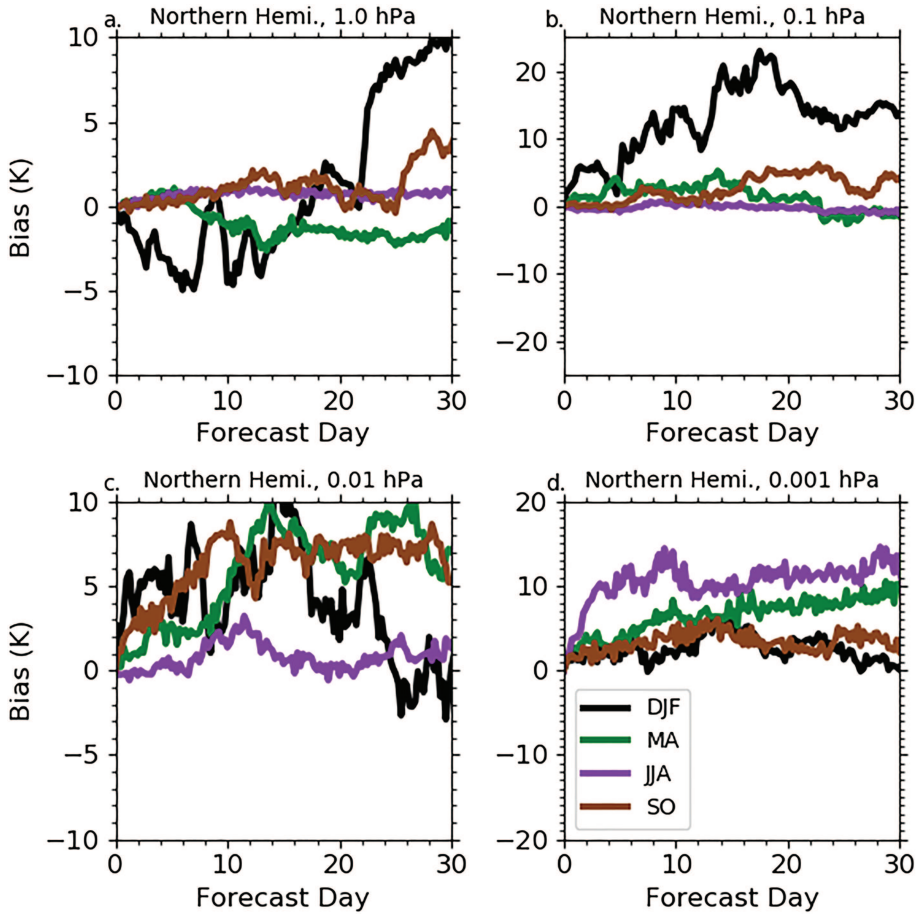

Figure 12. Northern Hemisphere (60–90° N) zonal mean temperature bias in WACCMX+DART hindcast experiments verified against WACCMX+DART analysis fields in different seasons at (a) 1.0, (b) 0.1, (c) 0.01, and (d) 0.001 hPa. Solid lines indicate the median of all hindcast experiments, and thick dashed line is the best fit error growth curve.

that could be improved in order to improve the error growth rates in the MLT. WACCMX+DART assimilates considerably fewer observations compared to a modern numerical weather prediction model and, in particular, does not assimilate satellite radiance observations, which significantly improved tropospheric weather prediction (e.g., Rabier, 2005). Though previous studies have demonstrated that WACCMX+DART analysis fields capture the large-scale dynamics (Gu et al., 2016; Gan et al., 2018; Pedatella et al., 2016), deficiencies in the observations assimilated in WACCMX+DART may shorten the forecast skill of the troposphere, subsequently influencing the forecast skill in the MLT. Additionally, the results may be impacted by the introduction of waves due to the data assimilation adjustments, and the additional damping that is included to mitigate the impact of these waves. Any spurious waves introduced by the data assimilation dissipate in the first few days of the hindcast experiments. As the model damping was adjusted to account for these waves, their absence in the hindcasts may influence the results. However, the extent to which this impacts the results is not currently known and requires additional investigation. Despite these short-comings, we believe that the WACCMX+DART hindcast experiments presented herein represent an important first investigation into the error growth rates at MLT altitudes.

There are additionally a number of limitations to the present study, which should be considered when interpreting the results. We have primarily verified the hindcast experiments by using the WACCMX+DART analysis fields. As the analysis fields are imperfect, especially at higher altitudes where there are only sparse observations, there is some uncertainty to the results. This is especially true for the small-scale waves, which are likely to be poorly constrained in the analysis fields. We have also not made use of the ensemble nature of the hindcasts and only considered the ensemble means. The ensembles may provide additional information that would be beneficial for forecasting the middle and upper atmosphere. Due to computational

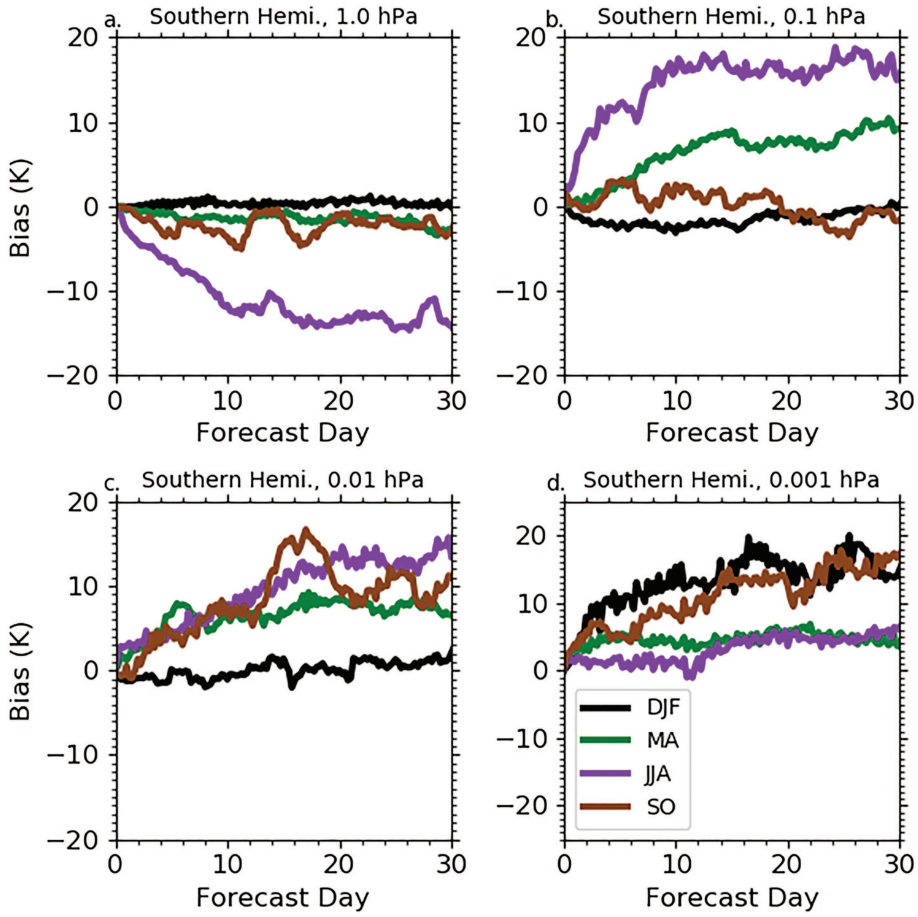

Figure 13. Same as Figure 12, except for the Southern Hemisphere (60–90° S).

constraints, the experiments were only performed for a 2-year time period and thus may not fully capture the seasonal differences in the error growth rates of the middle atmosphere. More extensive experiments are thus necessary to fully explore the seasonal dependencies. Last, it is important to emphasize that the results are based on only the current configuration of WACCMX+DART, and other models may perform differently. The results should therefore not be considered as definitive in terms of the error growth, predictability, and/or forecast skill of the MLT.

As the waves propagating upwards from the lower atmosphere are a considerable source of the ionosphere and thermosphere day-to-day variability, being able to forecast the middle atmosphere presents the opportunity to improve space weather forecasts, especially during geomagnetically quiet time periods. In extreme cases, such as SSW events, it has been shown that the ionosphere variability can be forecast up to roughly 1 week in advance (Pedatella et al., 2018; Wang et al., 2014). The results of the present study illustrate that at MLT altitudes, which are relevant for driving space weather, the errors saturate in WACCMX+DART after ~5 days, suggesting shorter average forecast skill compared to previous event studies that focused on SSWs. Event studies focusing on SSWs thus may not be entirely reflective of the typical behavior in terms of being able to forecast the MLT and ionosphere variability. On average, the errors in atmospheric tides in WACCMX+DART that drive much of the ionosphere electrodynamics also saturate after 2–5 days. The ability to leverage lower and middle atmosphere forecast skill to improve space weather forecasts may thus typically only provide a few days of forecast capability, at least based on the WACCMX+DART hindcast experiments considered in the present study. However, it is important to recognize that this is based on the average of the WACCMX+DART hindcast experiments, and specific time periods, such as SSW events, can potentially extend the forecast skill significantly. Identifying periods of enhanced MLT predictability is thus critical in order to understand the uncertainty in space weather forecasts that make use of whole atmosphere models.

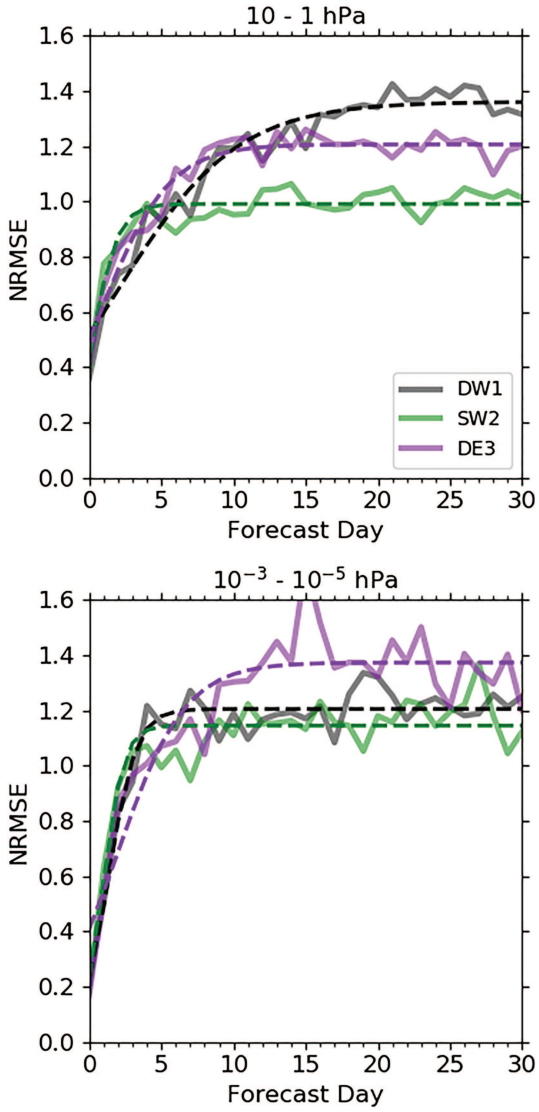

Figure 14. Normalized root mean square error for DW1, SW2, and DE3 temperatures in WACCMX+DART hindcast experiments verified against WACCMX+DART analysis fields. The root mean square error is calculated in the latitude ranges 20° S-20° N for DW1, 30° S-30° N for DE3, and 40° S-40° N for SW2. Results are shown for 10-1 hPa (top) and 10^{-3}-10^{-5} hPa (bottom). Solid lines indicate the median of all hindcast experiments, and thick dashed line is the best fit error growth curve.

It is important to also consider this result in light of the limitations of WACCMX+DART discussed in the previous paragraphs.

5. Conclusions

The present study investigates the error growth of the MLT based on an analysis of 47 initialized ensemble hindcast experiments in WACCMX+DART during 2009–2010. The results represent the first comprehensive investigation into the multiday error growth in the MLT and are useful for understanding how space weather forecasting may benefit from the use of whole atmosphere models. Whole atmosphere models can potentially benefit space weather forecasting by providing forecasts of the lower atmospheric drivers of ionosphere and thermosphere variability. The results demonstrate that in WACCMX+DART the error growth is slowest for the zonal mean and large scale waves and is significantly faster for small-scale waves. The time for the errors to reach saturation is also significantly shorter in the upper mesosphere and lower thermosphere compared to in the upper stratosphere and lower mesosphere. In the lower thermosphere, which

is an especially relevant altitude regime for driving ionosphere-thermosphere variability, the errors saturate in less than 5 days in WACCMX+DART. Errors in the migrating and nonmigrating atmospheric tides that drive much of the spatial and temporal day-to-day variability of the ionosphere also grow quickly in WACCMX+DART and reach saturation after ~2–5 days in WACCMX+DART.

We emphasize that the above conclusions are based on the current configuration of WACCMX+DART and do not represent inherent limits on the predictability and/or forecast skill of the MLT, or the behavior of other data assimilation systems. Rather, they represent the current capabilities of a single whole atmosphere model with data assimilation capabilities. Other models may have better or worse forecast skill in the MLT. Similar to tropospheric weather prediction (e.g., Bauer et al., 2015), we would also anticipate that future developments in the forecasting model, data assimilation techniques, and observations are likely to lead to enhanced forecasting capabilities in the MLT. How the ability to forecast the MLT influences ionospheric forecasts remains a topic for future research.

Acknowledgments
This material is based upon work supported by the National Center for Atmospheric Research, which is a major facility sponsored by the National Science Foundation under Cooperative Agreement No. 1852977. N. P. acknowledges support from National Science Foundation Grant AGS-1552153 and AGS-1033112, and NASA grant 80NSSC18K1046.. We would like to acknowledge high-performance computing support from Cheyenne (https://doi.org/10.5065/D6RX99HX) provided by NCAR's Computational and Information Systems Laboratory. The data used in this publication are available at https://doi.org/10.5065/27cw-q872. The WACCMX and DART software are open source community models available at http://www.cesm.ucar.edu/models/waccm-x/, and https://www.image.ucar.edu/DAReS/DART/, respectively.

References

Anderson, J. L. (2001). An ensemble adjustment Kalman filter for data assimilation. *Monthly Weather Review*, *129*(12), 2884–2903. https://doi.org/10.1175/1520-0493(2001)129<2884:aeakff>2.0.co;2

Anderson, J. L. (2009). Spatially and temporally varying adaptive covariance inflation for ensemble filters. *Tellus*, *61*, 72–83. https://doi.org/10.3402/tellusa.v61i1.15524

Anderson, J. L., Hoar, T., Raeder, K., Liu, H., Collins, N., Torn, R., & Arellano, A. F. (2009). The Data Assimilation Research Testbed: A community data assimilation facility. *Bulletin of the American Meteorological Society*, *90*, 1283–1296. https://doi.org/10.1175/2009BAMS2618.1

Bauer, P., Thorpe, A., & Brunet, G. (2015). The quiet revolution of numerical weather prediction. *Nature*, *525*(7567), 47–55. https://doi.org/10.1038/nature14956

Cash, M. D., Biesecker, D. A., Pizzo, V., de Koning, C. A., Millward, G., Arge, C. N., et al. (2015). Ensemble modeling of the 23 July 2012 coronal mass ejection. *Space Weather*, *13*, 611–625. https://doi.org/10.1002/2015SW001232

Dalcher, A., & Kalnay, E. (1987). Error growth and predictability in operational ECMWF forecasts. *Tellus A*, *39A*(5), 474–491. https://doi.org/10.1111/j.1600-0870.1987.tb00322.x

Eckermann, S. D., Hoppel, K. W., Coy. L., McCormack, J. P., Siskind, D. E., Nielsen, K., et al. (2009). High-altitude data assimilation system experiments for the northern summer mesosphere season of 2007. *Journal of Atmospheric and Solar-Terrestrial Physics*, *71*(3–4), 531–551. https://doi.org/10.1016/j.jastp.2008.09.036

Eckermann, S. D., Ma, J., Hoppel, K. W., Kuhl, D. D., Allen, D. R., Doyle, J. A., et al. (2018). High-altitude (0-100 km) Global Atmospheric Reanalysis System: Description and application to the 2014 Austral Winter of the Deep Propagating Gravity Wave Experiment (DEEPWAVE). *Monthly Weather Review*, *146*(8), 2639–2666. https://doi.org/10.1175/MWR-D-17-0386.1

Fang, T.-W., Akmaev, R., Fuller-Rowell, T., Wu, F., Maruyama, N., & Millward, G. (2013). Longitudinal and day-to-day variability in the ionosphere from lower atmosphere tidal forcing. *Geophysical Research Letters*, *40*, 2523–2528. https://doi.org/10.1002/grl.50550

France, J. A., Randall, C. E., Lieberman, R. S., Harvey, V. L., Eckermann, S. D., Siskind, D. E., et al. (2018). Local and remote planetary wave effects on polar mesospheric clouds in the Northern Hemisphere in 2014. *Journal of Geophysical Research: Atmospheres*, *123*, 5149–5162. https://doi.org/10.1029/2017JD028224

Gan, Q., Oberheide, J., & Pedatella, N. M. (2018). Sources, sinks, and propagation characteristics of the quasi 6-day wave and its impact on the residual mean circulation. *Journal of Geophysical Research: Atmospheres*, *123*, 9152–9170. https://doi.org/10.1029/2018JD028553

Garcia, R. R., Smith, A. K., Kinnison, D. E., Camara, A. d., & Murphy, D. J. (2017). Modification of the gravity wave parameterization in the Whole Atmosphere Community Climate Model: Motivation and results. *Journal of the Atmospheric Sciences*, *74*, 275–291. https://doi.org/10.1175/JAS-D-16-0104.1

Glocer, A., Rastätter, L., Kuznetsova, M., Pulkkinen, A., Singer, H. J., Balch, C., et al. (2016). Community-wide validation of geospace model local K-index predictions to support model transition to operations. *Space Weather*, *14*, 469–480. https://doi.org/10.1002/2016SW001387

Gu, S.-Y., Liu, H.-L., Pedatella, N. M., Dou, X., Li, T., & Chen, T. (2016). The quasi-2 day wave activities during 2007 austral summer period as revealed by Whole Atmosphere Community Climate Model. *Journal of Geophysical Research: Space Physics*, *121*, 2743–2754. https://doi.org/10.1002/2015JA022225

Hagan, M. E., Häusler, K., Lu, G., Forbes, J. M., & Zhang, X. (2015). Upper thermospheric responses to forcing from above and below during 1-10 April 2010: Results from an ensemble of numerical simulations. *Journal of Geophysical Research: Space Physics*, *120*, 3160–3174. https://doi.org/10.1002/2014JA020706

Hoffmann, P., Singer, W., Keuer, D., Hocking, W. K., Kunze, M., & Murayama Y. (2007). Latitudinal and longitudinal variability of mesospheric winds and temperatures during stratospheric warming events. *Journal of Atmospheric and Solar-Terrestrial Physics*, *69*, 2355–2366.

Hoppel, K. W., Baker, N. L., Coy, L., Eckermann, S. D., McCormack, J. P., Nedoluha, G. E., & Siskind, D. E. (2008). Assimilation of stratospheric and mesospheric temperatures from MLS and SABER into a global NWP model. *Atmospheric chemistry and physics, Discussions*, *8*, 8455–8490. https://doi.org/10.5194/acpd-8-8455-2008

Hoppel, K. W., Eckermann, S. D., Coy, L., Nedoluha, G. E., Allen, D. R., Swadley, S. D., & Baker, N. L. (2013). Evaluation of SSMIS upper atmosphere sounding channels for high-altitude data assimilation. *Monthly Weather Review*, *141*, 3314–3330. https://doi.org/10.1175/MWR-D-13-00003.1

Hurrell, J. W., Hack, J. J., Shea, D., Caron, J. M., & Rosinski, J. (2008). A new sea surface temperature and sea ice boundary dataset for the Community Atmosphere Model. *Journal of Climate*, *21*, 5145–5153.

Karpechko, A. Y. (2018). Predictability of sudden stratospheric warmings in the ECMWF extended-range forecast system. *Monthly Weather Review*, *146*, 1063–1075. https://doi.org/10.1175/MWR-D-17-0317.1

Kleinknecht, N. H., Espy P. J., & Hibbins R. E. (2014). The climatology of zonal wave numbers 1 and 2 planetary wave structure in the MLT using a chain of Northern Hemisphere SuperDARN radars. *Journal of Geophysical Research: Atmospheres*, *119*, 1292–1307. https://doi.org/10.1002/2013JD019850

Lauritzen, P. H., Mirin, A. A., Truesdal, J., Raeder, K., Anderson, J. L., Bacmeister, J., & Neale, R. B. (2012). Implementation of new diffusion/ filtering operators in the CAM-FV dynamical core. *International Journal of High Performance Computing Applications*, *26*, 63–73. https://doi.org/10.1177/1094342011410088

Lieberman, R. S., Riggin, D. M., Ortland, D. A., Oberheide, J., & Siskind, D. E. (2015). Global observations and modeling of nonmigrating diurnal tides generated by tide-planetary wave interactions. *Journal of Geophysical Research: Atmospheres*, *120*, 11,419–11,437,. https://doi.org/10.1002/2015JD023739

Liemohn, M., Ganushkina, N. Y., De Zeeuw, D. L., Rastaetter, I., Kuznetsova, M., Welling, D. T., et al. (2018). Real-time SWMF at CCMC: Assessing the Dst output from continuous operational simulations. *Space Weather*, *16*, 1583–1603. https://doi.org/10.1029/2018SW001953

Liu, H. L. (2016). Variability and predictability of the space environment as related to lower atmosphere forcing. *Space Weather*, *14*, 634–658. https://doi.org/10.1002/2016SW001450

Liu, H.-L., Bardeen, C. G., Foster, B. T., Lauritzen, P., Liu, J., Lu, G., et al. (2018). Development and validation of the Whole Atmosphere Community Climate Model with thermosphere and ionosphere extension. *Journal of Advances in Modeling Earth Systems*, *10*, 381–402. https://doi.org/10.1002/2017MS001232

Liu, H.-L., Sassi, F., & Garcis, R. R. (2009). Error growth in a Whole Atmosphere Climate Model. *Journal of the Atmospheric Sciences*, *66*, 173–186.

Liu, H. L., Talaat, E. R., Roble, R. G., Lieberman, R. S., Riggin, D. M., & Yee, J. H. (2004). The 6.5-day wave and its seasonal variability in the middle and upper atmosphere. *Journal of Geophysical Research*, *109*, D21112. https://doi.org/10.1029/2004JD004795

Marsh, D. R., Mills, M. J., Kinnison, D. E., Lamarque, J.-F., Calvo, N., & Polvani, L. M. (2013). Climate change from 1850 to 2005 simulated in CESM1(WACCM). *Journal of Climate*, *26*, 7372–7391. https://doi.org/10.1175/JCLI-D-12-00558.1

McDonald, A. J., Hibbins, R. E., & Jarvis, M. J. (2011). Properties of the quasi 16 day wave derived from EOS MLS observations. *Journal of Geophysical Research*, *116*, D06112. https://doi.org/10.1029/2010JD014719

Merkin, V. G., Owens, M. J., Spence, H. E., Hughes, W. J., & Quinn, J. M. (2007). Predicting magnetospheric dynamics with a coupled Sun-to-Earth model: Challenges and first results. *Space Weather*, *5*, S12001. https://doi.org/10.1029/2007SW000335

Morley, S. K., Welling, D. T., & Woodroffe, J. R. (2018). Perturbed input ensemble modeling with the space weather modeling framework. *Space Weather*, *16*, 1330–1347. https://doi.org/10.1029/2018SW002000

Neale, R. B., Richter, J. H., Park, S., Lauritzen, P. H., Vavrus, S. J., Rasch, P. J., & Zhang, M. (2013). The mean climate of the Community Atmosphere Model (CAM4) in forced SST and fully coupled experiments. *Journal of Climate*, *26*, 5150–5168. https://doi.org/10.1175/JCLI-D-12-00236.1

Nezlin, Y., Rochon, Y. J., & Polavarapu, S. (2009). Impact of tropospheric and stratospheric data assimilation on mesospheric prediction. *Tellus*, *61A*, 154–59. https://doi.org/10.1111/j.1600-0870.2008.00368.x

Owens, M. J., Horbury, T. S., Wicks, R. T., McGregor, S. L., Savani, N. P., & Xiong, M. (2014). Ensemble downscaling in coupled solar wind-magnetosphere modeling for space weather forecasting. *Space Weather*, *12*, 395–405. https://doi.org/10.1002/2014SW001064

Pedatella, N. M., & Liu, H.-L. (2018). The influence of internal atmospheric variability on the ionosphere response to a geomagnetic storm. *Geophysical Research Letters*, *45*, 4578–4585. https://doi.org/10.1029/2018GL077867

Pedatella, N. M., Liu, H.-L., Marsh, D. R., Raeder, K., Anderson, J. L., Chau, J. L., et al. (2018). Analysis and hindcast experiments of the 2009 sudden stratospheric warming in WACCMX+DART. *Journal of Geophysical Research: Space Physics*, *123*, 3131–3153. https://doi.org/10.1002/2017JA025107

Pedatella, N. M., Oberheide, J., Sutton, E. K., Liu, H.-L., Anderson, J. L., & Raeder, K. (2016). Short-term nonmigrating tide variability in the mesosphere, thermosphere, and ionosphere. *Journal of Geophysical Research: Space Physics*, *121*, 3621–3633. https://doi.org/10.1002/2016JA022528

Pedatella, N. M., Raeder, K., Anderson, J. L., & Liu, H.-L. (2014). Ensemble data assimilation in the Whole Atmosphere Community Climate Model. *Journal of Geophysical Research: Atmospheres*, *119*, 9793–9809. https://doi.org/10.1002/2014JD021776

Polavarapu, S., Ren, S., Rochon, Y., Sankey, D., Ek, N., Koshyk, J., & Tarasick, D. (2005). Data assimilation with the Canadian middle atmosphere model. *Atmosphere-Ocean*, *43*, 77–100. https://doi.org/10.3137/ao.430105

Rabier, F. (2005). Overview of global data assimilation developments in numerical weather-prediction centres. *Quarterly Journal of the Royal Meteorological Society*, *131*, 3215–3233. https://doi.org/10.1256/qj.05.129

Ren, S., Polavarapu, S., Beagley, S. R., Nezlin, Y., & Rochon, Y. J. (2011). The impact of gravity wave drag on mesospheric analyses of the 2006 stratospheric major warming. *Journal of Geophysical Research*, *116*, D19116. https://doi.org/10.1029/2011JD015943

Savijarvi, H. (1995). Error growth in large numerical forecast system. *Monthly Weather Review*, *123*, 212–221.

Shepherd, T. G., Koshyk, J. N., & Ngan, K. (2000). On the nature of large–scale mixing in the stratosphere and mesosphere. *Journal of Geophysical Research*, *105*(D10), 12,433–12,446. https://doi.org/10.1029/2000JD900133

Siscoe, G., & Solomon, S. C. (2006). Aspects of data assimilation peculiar to space weather forecasting. *Space Weather*, *4*, S04002. https://doi.org/10.1029/2005SW000205

Siskind, D. E., Stevens, M. H., Hervig, M., Sassi, F., Hoppel, K., Englert, C. R., & Kochenash, A. J. (2011). Consequences of recent Southern Hemisphere winter variability on polar mesospheric clouds. *Journal of Atmospheric and Solar-Terrestrial Physics*, *73*, 2013–2021. https://doi.org/10.1016/j.jastp.2011.06.014

Smith, A. K., Pedatella, N. M., Marsh, D. R., & Matsuo, T. (2017). On the dynamical control of the mesosphere-lower thermosphere by the lower and middle atmosphere. *Journal of the Atmospheric Sciences*, *74*, 933–947. https://doi.org/10.1175/JAS-D-16-0226.1

Sooraj, K. P., Annamalai, H., Kumar, A., & Wang, H. (2012). A comprehensive assessment of CFS seasonal forecasts over the tropics. *Weather Forecasting*, *27*(1), 3–27. https://doi.org/10.1175/waf-d-11-00014.1

Tripathi, O. P., Baldwin, M., Charlton-Perez, A., Charron, M., Eckermann, S. D., Gerber, E., et al. (2015). The predictability of the extratropical stratosphere on monthly time-scales and its impact on the skill of tropospheric forecasts. *Quarterly Journal of the Royal Meteorological Society*, *141*, 987–1003. https://doi.org/10.1002/qj.2432

Wang, H., Akmaev, R. A., Fang, T.-W., Fuller-Rowell, T. J., Wu, F., Maruyama, N., & Iredell, M. D. (2014). First forecast of a sudden stratospheric warming with a coupled whole-atmosphere/ionosphere model IDEA. *Journal of Geophysical Research: Space Physics*, *119*, 2079–2089. https://doi.org/10.1002/2013JA019481

Wang, H., Fuller-Rowell, T. J., Akmaev, R. A., Hu, M., Kleist, D. T., & Iredell, M. D. (2012). First simulations with a whole atmosphere data assimilation and forecast system: The January 2009 major sudden stratospheric warming. *Journal of Geophysical Research*, *116*, A12321. https://doi.org/10.1029/2011JA017081

Zülicke, C., Becker, E., Matthias, V., Peters, D. H., Schmidt, H., Liu, H., et al. (2018). Coupling of stratospheric warmings with mesospheric coolings in observations and simulations. *Journal of Climate*, *31*, 1107–1133. https://doi.org/10.1175/JCLI-D-17-0047.1